Hybrid manufacturing by 3D printing: A facile route to fabricate high-performance complex parts of low-fluidity high-entropy alloys

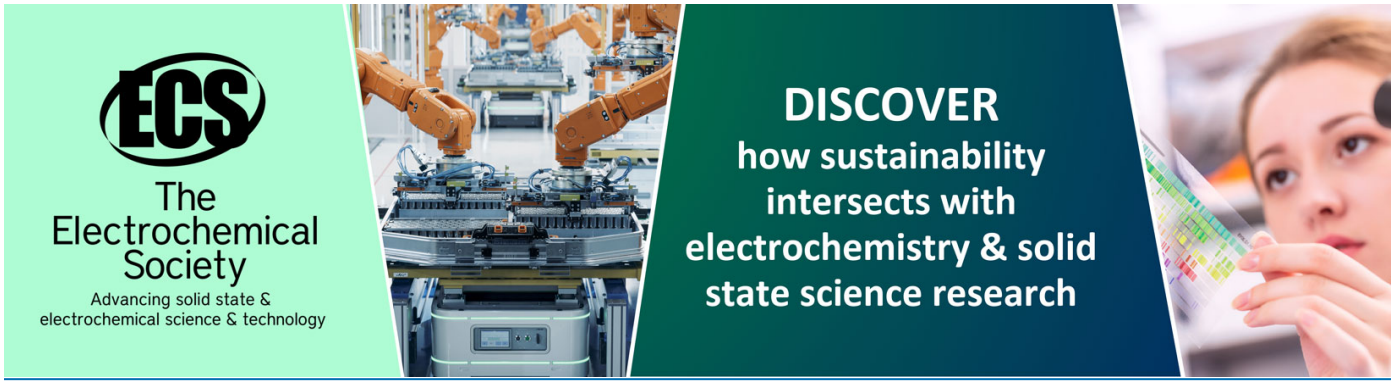

Hybrid manufacturing by 3D printing: A facile route to fabricate high-performance complex parts of low-fluidity high-entropy alloys

Yingmin Li[1], Yunkai Li[1a], Yichao Zhu[1b], Yao Xiao[1c], Yao-Jian Liang[1, *], Yunfei Xue[1d], Lu Wang[1e]

[1]School of Materials Science and Engineering, Beijing Institute of Technology, Beijing 100081, People's Republic of China.

*Corresponding author. E-mail address: liangyj@bit.edu.cn (Yao-Jian Liang)

First author. E-mail address: lymadvance@163.com (Yingmin Li)

[1a]liyunkai@bit.edu.cn, [1b]2268981459@qq.com, [1c]freelyxy@126.com, [1e]xueyunfei@bit.edu.cn, [1e]WangLu@bit.edu.cn

Abstract: For low-fluidity alloys such as TiNb-rich high-entropy alloys, casting parts with complex geometry normally encounter the forming problems like incomplete filling, shrinkage cavities and porosity. Additive manufacturing (AM) is suitable for fabricating those complex parts. However, for the regular portion of a complex part such as the disc o f an impeller, AM is not a cost-optimal choice. This work proposes a facile route to fabricate high-performance parts with complex geometry, in which the portion with regular geometry is cast whereas the complex portion that requires high performance is additively manufactured. The results show that the failure always occurs in the cast portion of the hybrid manufactured sample rather than at the interface between the AM portion and the cast one. The strong interfacial bonding is quite different from the welding joint which is commonly the weak link. Moreover, compared with the cast portion with coarse equiaxed grains, the equiaxed fine-grained AM portion exhibits higher strength without sacrificing ductility. Hybrid manufacturing does not introduce weakness, but rather can strengthen the targeted portion by a reasonable structural design.

1. Introduction

The fabrication of high-performance and complex parts is challenging, especially for low-fluidity alloys such as TiNb-rich high-entropy alloys (HEAs)[3, 6, 11-15]. Casting of these low-fluidity alloys frequently encounters forming problems like incomplete filling, shrinkage cavities, and porosity, which seriously degenerate the performance of the final parts. A valid way to produce dense parts is deformation processing such as forging and rolling. However, for these TiNb-rich alloys, deformation processing is usually conducted at high temperatures to obtain good processability. Such processing conditions require specific surface protection because of their poor oxidation resistance. More importantly, the production of parts with complex geometry needs a lot of machining works after deformation, which decreases the use of unprocessed materials with greatly increases the price.

AM/3D printing is able to fabricate complex parts in an argon gas chamber. During AM, high-performance parts with complex geometry can be fabricated layer-by-layer according to their computer-aided-design models[7]. The two advantages can effectively solve the forming problems resulting from low fluidity and poor oxidation resistance of these TiNb-rich alloys. However, a complex part often

consists of the portions with simple/regular geometry and the complex ones. For the regular parts (or regular portions of a part) such as the disc of an impeller, AM is not the cost-optimal choice. Accordingly, if the simple/regular portion of the part is cast (forged also) whereas the complex portions of the part are additively manufactured, high-performance complex parts with high material utilization and low cost can be fabricated easily[2, 5, 7]. For example, the vanes can be directly additively manufactured on the cast disc to obtain the complete impeller as schematically shown in Fig. 1.

To verify the feasibility of the hybrid manufacturing (HM) of high-performance complex parts with low-fluidity alloys, this work selects a low-fluidity TiNb-rich HEA (named as T50 hereinafter), and designs a HM sample to evaluate its properties. Additionally, the microstructure, hardness distribution and phase evolution were investigated to understand the properties evolution throughout the HM sample.

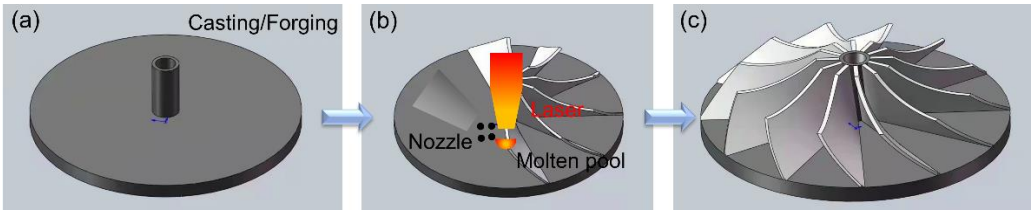

Fig. 1. Schematics of HM of a high-performance, complex part, using an impeller as the example.

2. Materials and methods

The AM was directly performed on a T50 cast ingot by a RC-LDM4030 laser additive manufacturing system (RAYCHAM Laser Technology Group Co. Ltd.) in an argon atmosphere with the oxygen content below 50 ppm. The raw T50 spherical powder was fabricated by gas atomization process with particle size distribution of 75-150 μm as shown in Fig. 2(a) and the T50 powder was delivered into the chamber through nozzle under argon gas at a powder feeding rate of 10-11 g/min. The AM parameters are as follows: laser power (P) of 1400 W, laser scanning speed (V_b) of 600 mm/min. The laser scanning method is back and forth multi-channel scanning with adjacent tracks on the opposite paths. The HM sample which consists of a 30 mm × 30 mm × 25 mm cast portion and a 20 mm × 20 mm × 25 mm AM portion was prepared (Fig. 2(b)). The HM sample was heat treated at 950 ℃ for 60 min and then cooled in water.

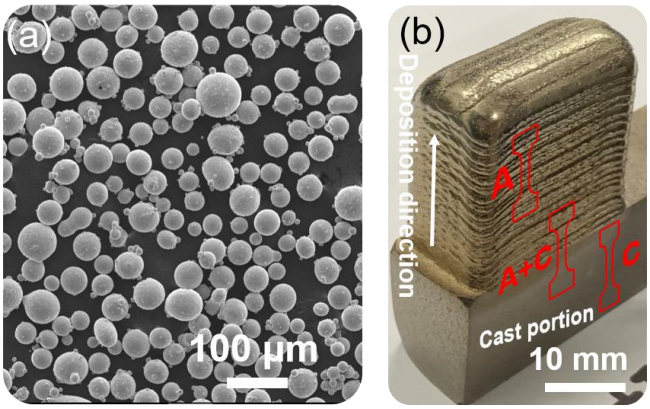

Fig. 2.(a) Morphology of T50 spherical powder. (b) The HM sample and the sampling positions of tensile samples.

The tensile samples were subjected to tensile tests on the CMT4105 electronic universal testing machine at a constant strain according to GB/T228.1-2010. For comparison, three different positions of tensile samples were selected: sample A, sample C and sample A+C with the interface in the middle. In Fig. 2(b), the samples A, C and A+C reflect the properties of AM, cast and HM samples, respectively.

The phase constituent was examined by synchrotron-based high energy X-ray diffraction (HEXRD)

technology. The beam was carried out to scan from the cast portion to the AM portion in 5 mm steps. The beam size was 200 × 200 μm², and the wavelength of the X-ray beam was 0.1173 Å.

The preparation of metallographic samples was firstly polished with SiC sandpapers, then polished with 1:5 Silica polishing suspension: H_2O polishing solution. Finally, the metallographic samples were etched by means of a corrosive agent with a ratio of 20% HNO_3+40% HF +40% H_2O (volume fraction) acid. The microstructure was characterized by optical microscopy (OM, ZEISS Stemi-508) and scanning electron microscope (SEM, ZEISS Gemini SEM 300). The grain morphology and orientation were characterized by electron backscatter diffraction (EBSD). The EBSD was carried out using HITACHI S4800 with 1 μm scanning step and the results were processed by the Channel 5 system. Vickers microhardness (Hv) was characterized by using JMHVS-50AT hardness tester with 5 kgf load and 10 s loading time. The loading direction was parallel to the deposition direction and each position spaced 4 mm. At least three points were selected in each position to ensure accuracy.

3. Results and discussion

3.1. The properties evolution throughout the HM sample

Fig. 3(a) shows the macro-morphology of grains and the hardness distribution throughout the HM sample. In Fig. 3(a), no obvious defects are found in the macro-morphology throughout the HM sample and no pore, crack, unfused particles are found at the interface in Fig. 3(b). The hardness in the AM portion (285±12 Hv) is higher than the cast one (260±8 Hv) in Fig. 3(a), and the positions near the interface exhibit a continuous change in hardness. The hardness change is related to chemical compositions, phase and grain size. To identify whether the hardness change is caused by chemical compositions, the EDS analysis was conducted. Table 1 shows the chemical compositions of the HM sample. The results show that the elemental composition of each portion is close to the design ratio, and the hardness change is not caused by chemical compositions.

Table 1 Chemical compositions (in at.%) in each portion.

Area	Ti	Zr	V	Nb	Al
AM portion	50.55±0.57	18.67±0.21	10.79±0.02	15.14±0.36	4.84±0.19
Interface	50.35±0.75	19.32±1.43	10.90±0.06	15.33±1.88	4.60±0.15
Cast portion	50.13±1.05	20.26±2.45	10.88±0.22	14.29±1.72	4.42±0.32

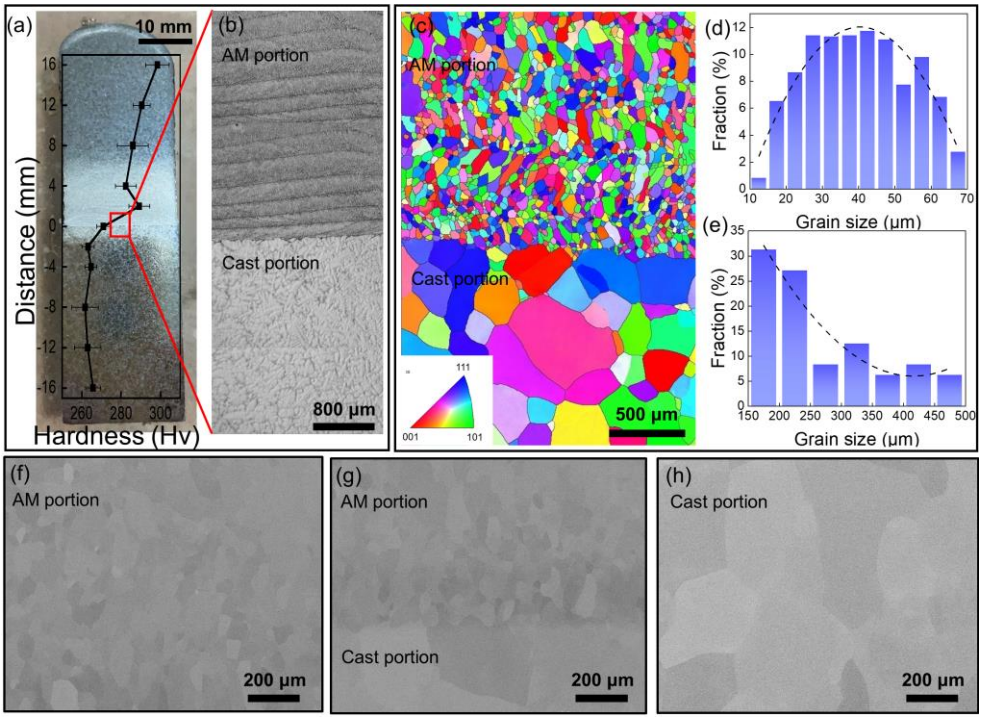

Fig. 3. (a) The macro-morphology and hardness distribution throughout the HM sample. The OM image (b) and EBSD IPF map (c) show the positions containing the interface between the cast portion and AM portion. Grain size distribution of the AM portion (d) and cast portion (e). The SEM-BSE images of (f)-(h) correspond to the different positions: (f) AM portion, (g) interface, (h) cast portion.

The Fig. 3(c) demonstrates that the HM sample is composed of equiaxed grains with random grain orientation and the mean grain size of AM portion (~46 μm) is much smaller than the cast one (~170 μm) (Fig. 3(d) and (e)). The development mechanism of equiaxed grains in the AM portion is discussed. During AM, the morphology of the grains of a given alloy is decided by the competitive growth of the equiaxed grains and columnar grains, which highly depend on the constitutional undercooling ahead of the solid/liquid (S/L) interface (ΔT_c)[9-10]. In general, a large ΔT_c is beneficial to the equiaxed growth ahead of the S/L interface, contributing to the formation of an equiaxed fine-grained microstructure[8]. The Fig. 4 schematically shows the constitutional undercooling zones produced by the alloys with different solidification intervals. Z means the distance from the S/L interface. When the real temperature is less than solidification temperature (i.e. $T(Z) < T_{liquid}(Z)$), the constitutional undercooling zone will be established in front of the S/L interface. According to CET model by Gäumann[4], which is suitable for high growth rate (v) as followed:

$$\Delta T_c = \Delta T(av)^{\frac{1}{n}} \quad (1)$$

where ΔT is equilibrium liquid-solidus interval, both a and n are alloy constants. ΔT_c is positively correlated with ΔT_0. Therefore, an alloy that has a larger solidification interval results in a larger constitutional undercooling zone, which is beneficial to the equiaxed growth. The liquid-solidus interval of different alloys was calculated by the JMatPro™ (Sente Software company), the T50 HEA has a larger equilibrium liquid-solidus interval (ΔT_2=53 K) than Ti-6Al-4V (ΔT_1=4 K), and it is concluded that T50 HEA has a larger constitutional undercooling zone and possesses a strong formation trend of the equiaxed fine-grained microstructure. Therefore, under the common processing window of AM, the T50 HEA is composed entirely of equiaxed grains.

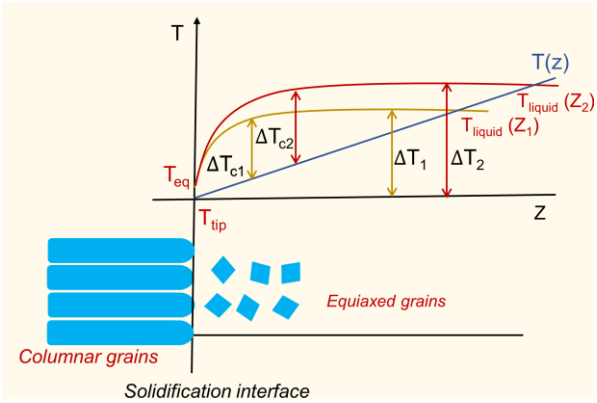

Fig. 4. Schematics of the constitutional undercooling zones produced by the alloys with different solidification intervals.

The notable precipitated phases are not found at the different positions of HM sample as shown in Fig. 3(f)-(h). To further identify whether the precipitated phases were produced during HM, the HEXRD analyses were conducted. Fig. 5 shows the HEXRD pattern of evolution of the reflection peaks with the positions from the cast portion to the AM portion. The results show that the phase of T50 HEA is BCC phase. In Fig. 5(a), several weak reflection peaks are found in the AM portion from 2.2° to 2.8° and 4.2° to 6.8°, implying that the precipitated phases were produced during AM. Thus, the heat treatment (HT) was conducted to dissolve the precipitated phases. After HT, only quite weak reflection peak at 4.8° to 5.4° remains as shown in Fig. 5(b). In summary, the most precipitated phases have been dissolved and the HM T50 after HT can be considered as a single-phase BCC HEA. As shown in Fig. 6(e)-(g), no precipitated phases are found at the different positions of the HM sample after HT.

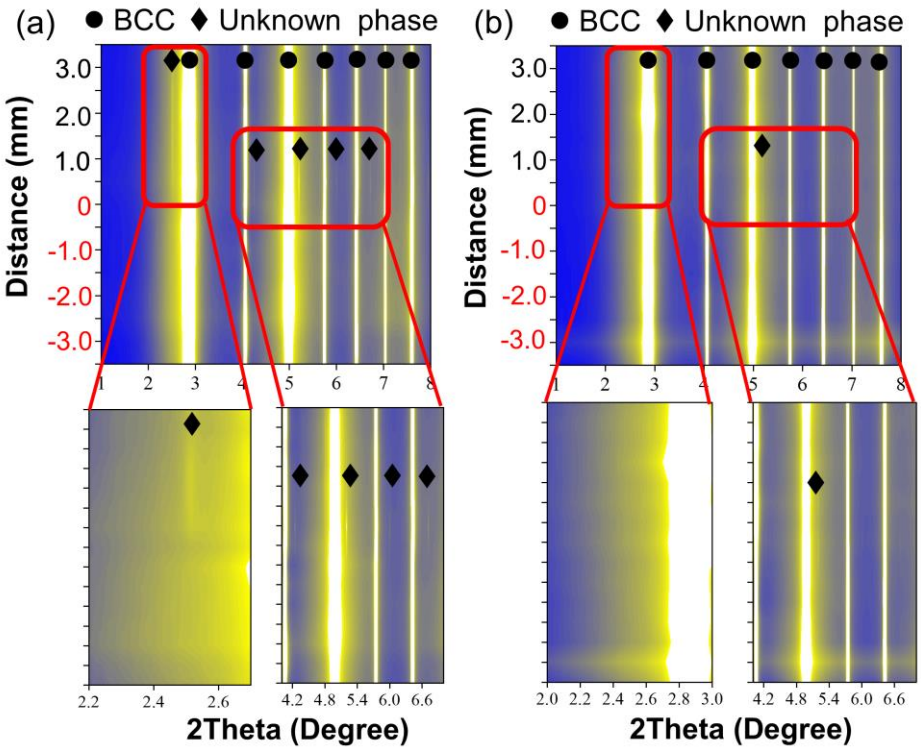

Fig. 5. The HEXRD pattern of the evolution of the reflection peaks of the HM sample before (a) and after (b) HT.

To identify whether the hardness change is caused by precipitated phases, the hardness of the HM

sample after HT was tested. Fig. 6(a) shows the hardness distribution throughout the HM sample after HT. No obvious change in hardness of the HM sample before and after HT, indicating that the hardness change is not due to the precipitated phases. Thus, the hardness change is caused by the grain size. As side by the Hall-Petch equation[1],

$$H_V = H_0 + {K_H}/{\sqrt{D}} \tag{2}$$

where the H_0 and K_H are alloying constants, H_V is the hardness and D is the grain size. The hardness is negatively correlated with grain size. Thus, the hardness of fine-grained AM portion is higher than coarse-grained cast portion. Compared with microstructure of the HM sample before HT, the grains keep equiaxed, but the fine grains grew up significantly in the AM portion (~75 μm) in Fig. 6(b), while the coarse grains in the cast portion have no visible change. (~185 μm) (Fig. 6(c) and (d)).

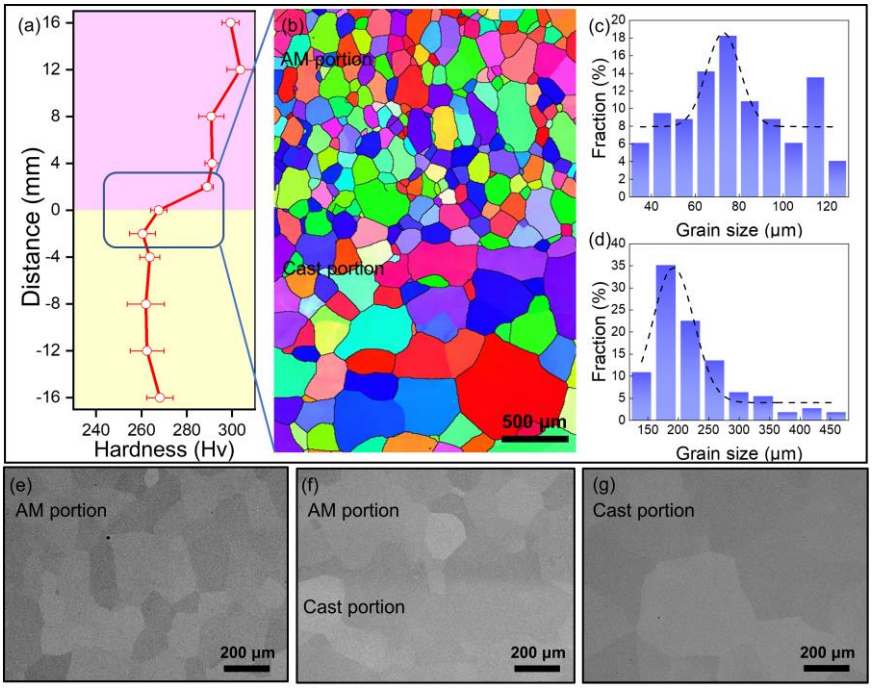

Fig. 6. (a) The hardness distribution throughout the HM sample after HT. (b) The EBSD IPF map shows the positions containing the interface between the cast portion and AM portion. Grain size distribution of the AM portion (c) and cast portion (d). The SEM-BSE images of (e)-(g) correspond to the different positions: (e) AM portion, (f) interface, (g) cast portion.

3.2. Mechanical properties

Fig. 7 shows the engineering stress-strain curves of the sample A, sample A+C and Sample C. In Fig. 7(a), the yield and ultimate strength of samples A is higher than the sample C. The higher strength of sample A than the sample C is due to the finer grain size. According to Hall-Petch equation(610 BataPereloma, 2004),

$$\sigma_y = \sigma_0 + {K_y}/{\sqrt{D}} \tag{3}$$

where the σ_0 and K_y are alloying constants, σ_y is the yield strength and D is the grain size. The yield strength is negatively correlated with grain size. Thus, the yield strength of AM portion is higher than that of the cast portion. The yield and ultimate strength of samples A+C is higher than the sample C. Compared with the elongation of sample A (12.8±1.51%) and sample C (16.3±1.37%), sample A+C exhibits the lowest elongation (8±1.06%). After HT, even though the strength of sample A decrease slightly (~20 MPa), the yield and ultimate strength of samples A and A+C are still higher than the sample C in Fig. 7(b). According to the summary of tensile properties in Fig. 8, the elongation of the samples

A, A+C and C have been increased after HT, and the elongation of sample A has increased due to the dissolution of most precipitated phases after HT.

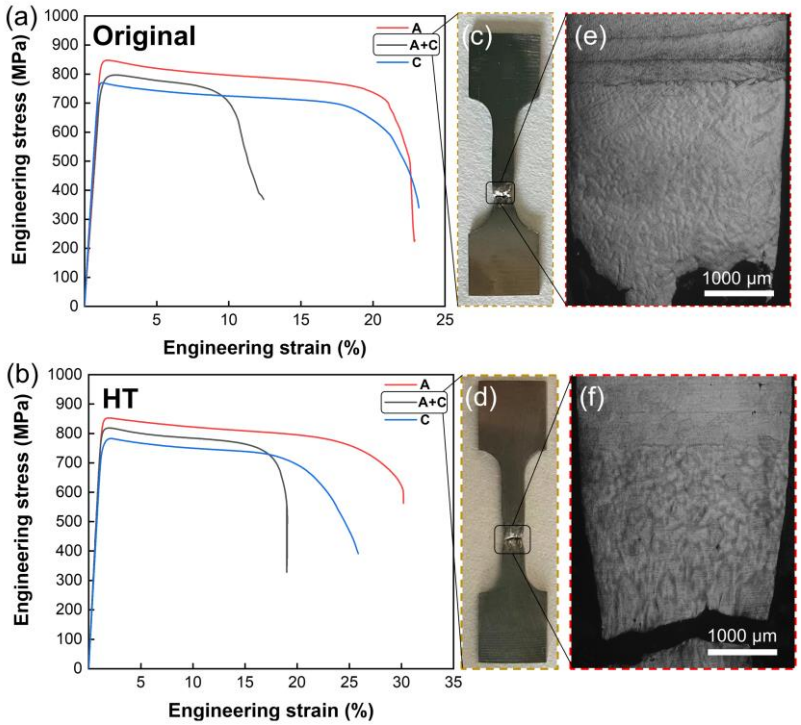

Fig. 7. Engineering stress-strain curves of the samples A, A+C, C before (a) and after (b) HT. Fracture positions of the samples A+C (c) and (d). (e) and (f) correspond to the high magnification OM images of fracture positions.

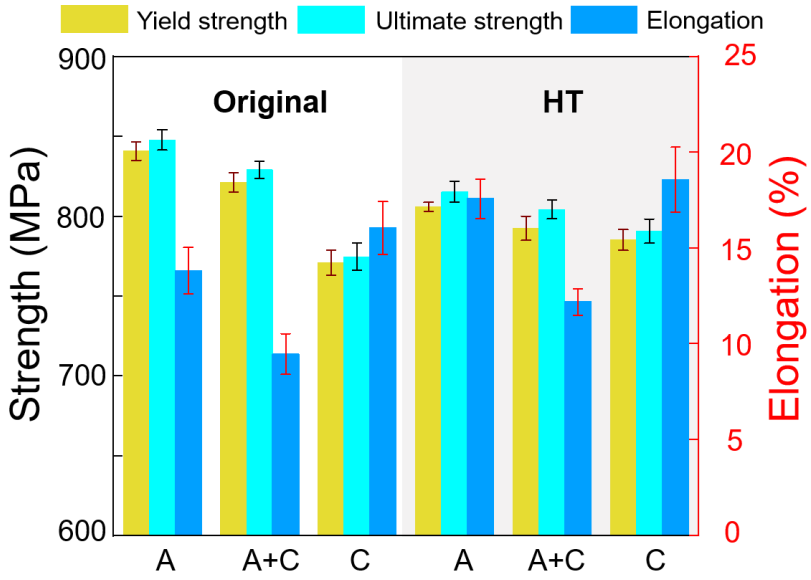

Fig. 8. Comparison of the tensile properties.

In Fig. 7(c)-(f), the fracture positions of all the samples A+C are in the cast portion, rather than at the interface between the AM portion and cast one, indicating that the interface has higher strength than the cast portion. The elongation and fracture positions of the sample A+C are discussed. The schematics of tensile test of sample A+C are shown in Fig. 9. The L_0 is the original gauge length, L_1 is the gage

length after fracture. ΔL_E is the gauge length difference in the elastic deformation stage, ΔL_P is the gauge length difference in the plastic deformation stage. In the sample A+C, ΔL_{AM} and ΔL_{cast} are the gauge length difference before and after tensile test in the AM portion and cast portion, respectively. According to the definition of elongation (EL):

$$EL = {\Delta L}/{L_0} \tag{4}$$

$$\Delta L = L_1 - L_0 = \Delta L_{AM} + \Delta L_{cast} \tag{5}$$

$$EL = {(\Delta L_{AM} + \Delta L_{cast})}/{L_0} \tag{6}$$

where the ΔL is gauge length difference before and after tensile test. During the tensile test with sample A+C, when the A half (i.e. the AM portion) is elastically deformed, the C half (i.e. the cast portion) will initially yield and start to plastically deform due to the lower yield strength. In Fig. 8, the ultimate tensile strength of sample C does not reach the yield strength of sample A so that C half of the sample A+C was subjected to almost all of the plastic deformation while no significant plastic deformation occurs in A half (i.e. $\Delta L_{AM} = 0$). Compared with two halves of sample C were subjected to plastic deformation at the same time, EL_C and EL_{A+C} have a relationship as:

$$EL_C = {2\Delta L_{cast}}/{L_0} = 2EL_{A+C} \tag{7}$$

This relationship is accordance with the results in Fig. 8. Therefore, the difference in strength between AM portion and cast one leads to the sample A+C exhibit the lowest ductility. Overall, the interface between the AM portion and the cast one is bonded strongly. These results indicate that the AM can produce a part/portion with the best properties, and hybrid manufacturing does not introduce weakness, but rather can strengthen the targeted portion by a reasonable structural design.

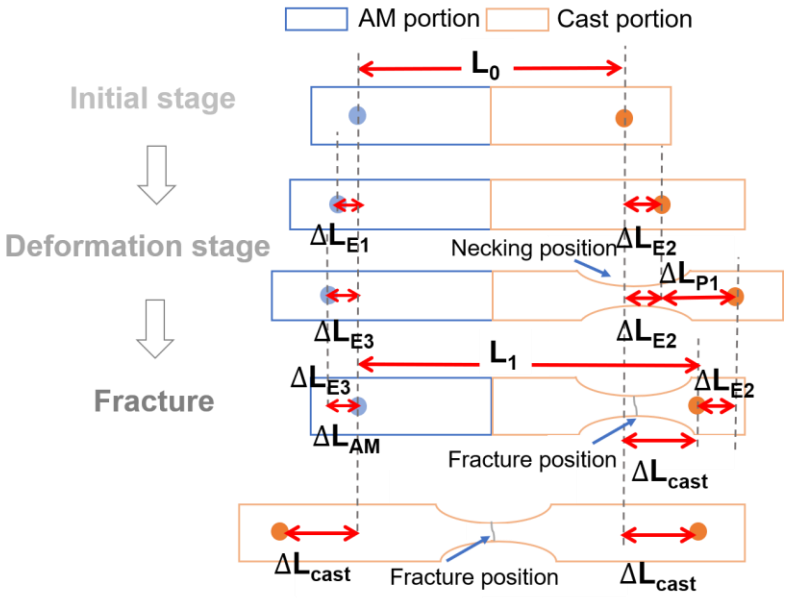

Fig. 9.Schematics of the tensile test of the sample A+C.

4. Conclusions

This work proposes a facile route to manufacture high-performance complex parts of low-fluidity alloys by consisting the AM and the conventional processing (e.g. casting), and a HM sample of the T50 HEA was manufactured to prove the feasibility of HM.

(1) The HM sample is composed of equiaxed fine-grained (~46 μm) and equiaxed coarse-grained

cast portion (~170 μm) due to the T50 HEA has a large constitutional undercooling zone.

(2) The AM samples have higher tensile strength than cast sample, indicating that AM can produce a part/portion with best properties and the hybrid manufacturing can strengthen the targeted portion by a reasonable structural design. The HM samples failure in the cast portion, indicating that the interface between the AM portion and the cast portion is strong, and unlike welding, HM does not produce weakness. The HM samples show the lowest elongation due to the different strength of AM portion and cast portion.

(3) The precipitated phases are found in the AM portion of the HM sample and can be effectively dissolved by HT. However, the grain growth of the AM portion during HT is also found, which means that system research on the HT of a HM sample is required for further improvement in the performance. Hybrid manufacturing can be readily extended to other low-fluidity alloys while meeting their complex geometry and high-performance requirements.

Acknowledgements:
This work was supported by National Priority Research and Development [Grant 2018 YFB0703400], National Natural Science Foundation [Grant 51901023], Beijing City Natural Science Foundation [Grant 2204094] and the Beijing Science Fund Program for Youth Scientist. The contract of Advanced Photon Source is No. DE-AC02-06CH11357.

References:

[1] Bata V, Pereloma E V.(2004) An alternative physical explanation of the Hall–Petch relation Acta Mater 52 657-65
[2] Cai C, Gao X, Teng Q, Li M, Pan K, Song B, Yan C, Wei Q, Shi Y.(2018) A novel hybrid selective laser melting/hot isostatic pressing of near-net shaped Ti-6Al-4V alloy using an in-situ tooling: Interfacial microstructure evolution and enhanced mechanical properties Mater. Sci. Eng. A 95-104
[3] Dong Y G, Chen S, Jia N N, Zhang Q H, Wang L, Xue Y F, Jin K. (2021) Microstructures and mechanical properties of Ta–Nb–Zr–Ti–Al refractory high entropy alloys with varying Ta/Ti ratios Tungsten
[4] G Umann M, Bezen On C, Canalis P, Kurz W. (2001) Single-crystal laser deposition of superalloys: processing–microstructure maps Acta Mater 49 1051-62
[5] Geng X, Mao X, Wu H H, Wang S, Xue W, Zhang G, Ullah A, Wang H. (2021) A hybrid machine learning model for predicting continuous cooling transformation diagrams in welding heat-affected zone of low alloy steels J Mater Sci Technol 207-215
[6] George E P, Raabe D, Ritchie R O. (2019) High-entropy alloys Nat Rev Mater 4 515-34
[7] Guan S, Wan D, Solberg K, Berto F. (2020) Additively manufactured CrMnFeCoNi/AlCoCrFeNiTi0.5 laminated high-entropy alloy with enhanced strength-plasticity synergy Scr. Mater 183 133-8
[8] Hunt J D.(1984) Steady state columnar and equiaxed growth of dendrites and eutectic Mater. Sci. Eng. 65 75-83
[9] Kurz W, Bezenon C, Gumann M. (2008) Columnar to equiaxed transition in solidification processing Sci Technol Adv Mat 2 185-91
[10] Lapin J, Klimová A, Gabalcová Z.(2013) Effect of columnar to equiaxed transition on microsegregation behaviour of main alloying elements in peritectic TiAl-based alloy Kovove Mater. 51 147-54
[11] Liang Y J, Li A, Cheng X, Pang X T, Wang H M.(2016) Prediction of primary dendritic arm spacing during laser rapid directional solidification of single-crystal nickel-base superalloys J. Alloys. Compd. 688 133-42
[12] Liang Y J, Liu D, Wang H M. (2014) Microstructure and mechanical behavior of commercial purity Ti/Ti–6Al–2Zr–1Mo–1V structurally graded material fabricated by laser additive manufacturing Scr. Mater 74 80-3

[13] Liang Y J, Tian X J, Zhu Y Y, Li J, Wang H M. (2014) Compositional variation and microstructural evolution in laser additive manufactured Ti/Ti–6Al–2Zr–1Mo–1V graded structural material Mater. Sci. Eng. A
[14] Liang Y, Li J, Li A, Cheng X, Wang S, Wang H. (2017) Experimental optimization of laser additive manufacturing process of single-crystal nickel-base superalloys by a statistical experiment design method J Alloy Compd 697 174-81
[15] M., Gäumann, R., Trivedi, W Kurz. (1997) Nucleation ahead of the advancing interface in directional solidification Mater. Sci. Eng. A